

Exchange bias of Ni nanoparticles embedded in an antiferromagnetic IrMn matrix

Q.1 **Balati Kuerbanjiang**¹, **Ulf Wiedwald**^{2,4}, **Felix Häring**²,
Q.2 **Johannes Biskupek**³, **Ute Kaiser**³, **Paul Ziemann**² and **Ulrich Herr**¹

¹ Institut für Mikro- und Nanomaterialien, Universität Ulm, Albert-Einstein-Allee 47, D-89081 Ulm, Germany

² Institut für Festkörperphysik, Universität Ulm, Albert-Einstein-Allee 11, D-89069 Ulm, Germany

³ Materialwissenschaftliche Elektronenmikroskopie, Universität Ulm, Albert-Einstein-Allee 11, D-89081 Ulm, Germany

E-mail: balati.kuerbanjiang@uni-ulm.de

Received 10 May 2013, in final form 22 August 2013

Published

Online at stacks.iop.org/Nano/24/000000

(Ed: Editor19)

Ascii/Word/NAN/
nano474235/PAP

Printed 1/10/2013

Spelling US

Issue no

Total pages

First page

Last page

File name

Date req

Artnum

Cover date

Abstract

Q.3 The magnetic properties of Ni nanoparticles (Ni-NPs) embedded in an antiferromagnetic IrMn matrix were investigated. The Ni-NPs of 8.4 nm mean diameter were synthesized by inert gas aggregation. In a second processing step, the Ni-NPs were *in situ* embedded in IrMn films or SiO_x films under ultrahigh vacuum (UHV) conditions. Findings showed that Ni-NPs embedded in IrMn have an exchange bias field $H_{EB} = 821$ Oe at 10 K, and 50 Oe at 300 K. The extracted value of the exchange energy density is 0.06 mJ m⁻² at 10 K, which is in good accordance with the results from multilayered thin film systems. The Ni-NPs embedded in SiO_x did not show exchange bias. As expected for this particle size, they are superparamagnetic at $T = 300$ K. A direct comparison of the Ni-NPs embedded in IrMn or SiO_x reveals an increase of the blocking temperature from 210 K to around 400 K. The coercivity of the Ni-NPs exchange coupled to the IrMn matrix at 10 K is 8 times larger than the value for Ni-NPs embedded in SiO_x. We studied time-dependent remanent magnetization at different temperatures. The relaxation behavior is described by a magnetic viscosity model which reflects a rather flat distribution of energy barriers. Furthermore, we investigated the effects of different field cooling processes on the magnetic properties of the embedded Ni-NPs. Exchange bias values fit to model calculations which correlate the contribution of the antiferromagnetic IrMn matrix to its grain size.

[S] Online supplementary data available from stacks.iop.org/Nano/24/000000/mmedia

Q.4 (Some figures may appear in colour only in the online journal)

1. Introduction

Q.5 Magnetic nanoparticles have huge potential for applications such as data storage [1], nano-sensors [2], biomedical diagnoses and therapy [3–6]. However, superparamagnetism limits the minimum size of the particles in many fields

which require a stable magnetization of the particles over time. One way to overcome this limit is to elicit exchange anisotropy by coupling ferromagnetic (FM) particles to antiferromagnetic (AF) surroundings, as demonstrated by Skumryev *et al* [7]. Until now, studies of exchange bias in nanoparticles have mainly concentrated on core-shell systems, such as ferromagnetic particle cores (Co, Ni, Fe) surrounded by their native oxide shells [8, 9]. This approach limits the selection of FM particles which can be studied.

⁴ Present address: Universität Duisburg-Essen Fakultät für Physik, Experimentalphysik-AG Farle, Lotharstrasse 1, D-47057 Duisburg, Germany.

Table 1. List of the parameters for the sample preparation. P_{base} gives the base pressure of the vacuum system. P_{proc} is the process gas (Ar) pressure. P , I and U are the power, current and voltage supplied to the sputter guns, respectively. The diameter of the Ni-NP sputter target is 2 in.

Parameters (units)	P_{base} (mbar)	P_{proc} (mbar)	Flow rate (sccm)	P (W)	I (mA)	U (V)	Thickness (nm)
IrMn	$<2 \times 10^{-7}$	5.4×10^{-3}	37	100	225 ± 10	450 ± 10	16
Ni-NP	$<2 \times 10^{-7}$	0.8	50	50	190 ± 10	265 ± 5	$\varnothing 8.4$

There have also been attempts to make exchange bias system by embedding Co particles in a Mn matrix, forming an AF shell by alloying Mn with Co at the interface by subsequent heat treatment [10]. So far, very few groups have tried to embed particles in metallurgically unrelated AF media without further reactions. In all cases studied previously [8–14], the values of the exchange bias field H_{EB} and coercivity H_{C} at room temperature are very low, with corresponding superparamagnetic blocking temperatures below room temperature, thus making such systems less attractive for applications. Different from most of the literature reports ([15, 16] and references therein), the present work is focusing on the interaction of Ni-NPs and IrMn films used as an embedding matrix. For this purpose, a combination of an inert gas aggregation process and IrMn film deposition was applied delivering well-separated Ni-NPs with negligible interaction among each other and narrow size distributions. The use of IrMn as an AF material appears particularly suited due to its high blocking temperature (400–540 K, depending on compositions and synthesis conditions [17, 18]), Néel temperature (as high as 690 K [18]) and its fairly good corrosion resistance, which are all important properties for practical applications.

The above addressed approach of stabilizing the magnetization fluctuations of nanoparticles is based on exchange bias, an effect discovered as early as 1956 [19], and the subject of extensive research work due to its application in GMR sensors [20]. Nevertheless, the theory describing the effect has still not been understood in all details. The exchange bias particle systems studied so far are mostly core–shell nanoparticles [8]. In the core–shell systems, however, there is a microstructural growth relation between the FM core and the AF oxide shell. Systems such as FM-NPs embedded in AF matrices without such a growth relation were rarely reported. In particular, to the best of our knowledge, there is no report about Ni nanoparticles embedded in IrMn films. Thus, in the present work, we have studied the temperature dependence of the exchange bias and relaxation behavior of Ni-NPs embedded in an IrMn matrix (volumetric filling fraction, $\text{VFF} = 3\%$) at temperatures between 10 and 400 K. Ni has a lower Curie temperature than Co, but also a lower magneto-crystalline anisotropy. One may, therefore, expect systems with Ni-NPs to react more sensitively to the influence of exchange anisotropy effects. By additionally comparing Ni-NPs of the same size but embedded in non-magnetic SiO_x films, we have been able to quantitatively trace back the change of the effective magnetic anisotropy of the Ni-NPs as induced by the particle–matrix interaction.

2. Experiments

We prepared Ni-NP@IrMn samples by *in situ* sequentially sputter depositing IrMn in the form of 16 nm thick layers, and depositing Ni-NPs using an inert gas aggregation cluster source [21]. Thicker samples with a larger magnetic signal of the Ni-NPs were formed by repeating the sequence of deposition steps 8 times. We used pieces of (100) Si wafers coated with 100 nm Si_3N_4 as substrates. Particles and layers were deposited on the substrate which was at ambient temperature. Preparation parameters are given in table 1. The target for IrMn deposition was made by patching a 2 in diameter Mn target with small Ir flakes. Since the AF properties of IrMn alloys strongly depend on the relative concentration of Ir (highest exchange energy densities were observed in the range of 15–35 at.% Ir [22]), we tuned the Ir concentration in the film to 26 at.%. We calibrated the deposition rate of the IrMn films by measuring the thickness of IrMn layers deposited over a given time by using x-ray reflectometry (not shown). Compositional and structural characterizations were carried out by EDX in a LEO 1550 SEM equipped with an Oxford INCA energy dispersive spectrometer using STRATAGEM analysis software, x-ray diffraction (XRD, Siemens D5005) and high-resolution transmission electron microscopy (HRTEM, FEI Titan 80-300), and by using energy filtered TEM (EFTEM) for local elemental analysis.

For the particle size measurement, we prepared another set of samples by deposition on holey carbon film covered TEM grids which were imaged in an SEM using transmission mode. This method has been found to be more accurate for nanoparticle diameter determination than the conventional imaging of particles with secondary electrons in standard SEM. Details of the measurements will be provided in a separate work. Here, the particle size and its distribution are important for the analysis of the magnetic data.

To induce exchange bias, we kept the as-prepared sample inside a superconducting quantum interference device (SQUID) magnetometer at 350 K for an hour under an applied field of 50 kOe. The resulting magnetic state is addressed as *reference state* hereafter. In a first set of experiments, the sample was cooled to 10 K under 50 kOe. Subsequently, a series of magnetization versus field (M – H) loops were recorded at several temperatures, ranging from 10 to 350 K. From these M – H loops, H_{C} and H_{EB} have been evaluated.

In addition, magnetization M versus temperature T curves were determined based on zero field cooled (ZFC) and field cooled (FC) protocols. The ZFC samples were cooled from 350 K down to 10 K without applied field. Subsequently, a small magnetic field (20 Oe) was applied in parallel to the

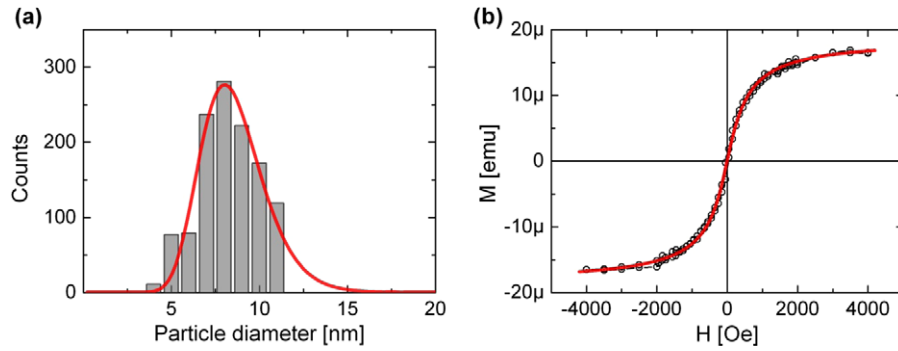


Figure 1. (a) Size distribution of non-embedded Ni-NPs from STEM images; the solid line is the log-normal fit. (b) The $M-H$ curve of the Ni-NP@SiO_x at ambient temperature. The red solid curve is a weighted average of Langevin functions calculated for the same size distribution of Ni-NPs as found in (a) (scaled to the same saturation value).

sample surface (in-plane geometry), and the zero field cooled magnetization was measured during heating up to 400 K. The FC samples were cooled from the *reference state* to 10 K in an applied field of 20 Oe. Afterwards, the field cooled magnetization was measured during heating. The results of these measurements are reported in section 3.2.

The long-time stability of the magnetization was characterized by FC thermo-relaxation measurements carried out after field cooling from the *reference state* to a temperature T_{fc} . After switching off the field, the remanent magnetization was recorded over typically 8 h. The results are shown in section 3.3.

The above described experimental procedures are well suited for obtaining a first overview of the magnetic properties of the Ni-NPs. However, it is well known that not only the ferromagnetic particles but also the antiferromagnetic film shows relaxation effects [23]. This implies that the results of the measurements may depend on details such as the measurement time, and the time intervals between the individual measurements after field cooling. For a quantitative modeling of the system of Ni-NPs in IrMn films, we have therefore performed a set of experiments using a different protocol. The sample was field cooled from the *reference state* to T_{fc} . At T_{fc} , the field was switched off and the sample was cooled further to 10 K, after which the hysteresis curve was recorded. By following this procedure we could largely eliminate the effect of relaxation processes after field cooling in the antiferromagnetic film. The results are presented in section 3.4.

For some samples, the measurements were repeated after storing the sample in ambient conditions for two months or one year, respectively. We have not observed any significant change in magnetic properties. After all measurements, x-ray photoemission spectroscopy (XPS) in combination with sputter depth profiling (using 5 keV Ar⁺ ions) was conducted to determine the chemical states of Ni in the sample for possible oxidation effects. Oxidation of Ni-NPs did not take place when the sample had been exposed to ambient conditions for two months. However, we have found some indication of a Mn segregation at the topmost IrMn layer, and an Ir rich lower part (5 nm from the surface) serving as a protective layer for the whole sample.

3. Results and discussion

3.1. Structure and morphology

The size and the shape of the nanoparticles synthesized by inert gas aggregation cluster sources mainly depend on the gas aggregation length, sputter power (current and voltage), gas pressure and flow, type of gas and the chamber geometry [24]. Identical parameters were applied for all samples (see table 1 for details), to achieve similar sized Ni particles. The average Ni-NP diameter extracted from analysis of the STEM images is 8.4 nm. The particle size distribution follows a log-normal distribution with $\sigma = 0.2$ as shown in figure 1(a). The $M-H$ curve of the Ni-NP@SiO_x recorded at ambient temperature shows superparamagnetic response (circles in figure 1(b)). This is expected for 8.4 nm diameter Ni-NPs according to the Arrhenius–Néel law,

$$\tau_N = \tau_0 e^{K_{\text{eff}} V / (k_B T)}, \quad (1)$$

in which τ_N is the Néel relaxation time at one orientation, $\tau_0 = 10^{-9}$ s, K_{eff} is the effective anisotropy constant of the material, V is the particle volume, k_B is the Boltzmann constant, and T is the temperature [25]. From this relation, we can derive a critical diameter of the particles or grains at a given measurement time, the so-called superparamagnetic limit. An estimate of the critical particle diameter D_s below which superparamagnetism sets in can be achieved by rearranging equation (1),

$$D_s = \left[\frac{6k_B T}{\pi K_{\text{eff}} \ln(t_{\text{meas}}/\tau_0)} \right]^{1/3}. \quad (2)$$

Here, t_{meas} is the measurement time. Using the K_{eff} of bulk Ni at 300 K [26], we obtain $D_s = 40$ nm for an average time of magnetization stability of 10 years, and $D_s = 35$ nm for 100 s, i.e. the typical observation time in SQUID magnetometry. According to these values, non-hysteric behavior of the magnetization is expected for our Ni-NPs at 300 K. The $M-H$ curve of superparamagnetic particles can be fit by a Langevin function,

$$M(H, T) = N\mu \left[\coth \left(\frac{\mu H}{k_B T} \right) - \frac{k_B T}{\mu H} \right]. \quad (3)$$

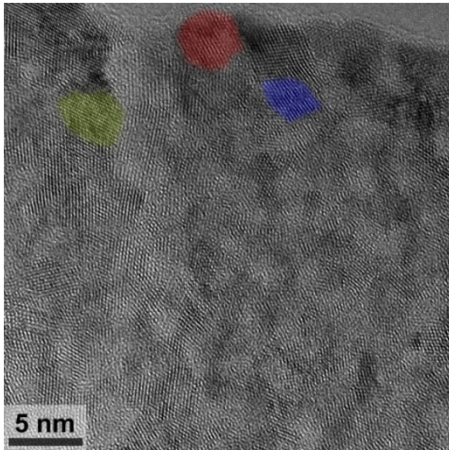


Figure 2. Cross section HRTEM images of Ni-NP@IrMn showing the polycrystalline IrMn matrix; some individual grains are shaded in color.

N is the number of particles, and μ the magnetic moment per particle. By comparison of Langevin functions calculated for a given particle size with the measured data, we can determine the magnetic particle size [27]. The magnetic Ni-NP size thus found was 8.5 nm (by using bulk values of Ni from [26], and the fit to the experimental data is shown in figure 1(b)), which agrees well with the particle size determination by STEM.

The microstructure of the IrMn films plays a major role in the strength of the exchange coupling. The areal exchange energy density, J_{ex} , is known to be proportional to the anisotropy of the antiferromagnet, K_{AF} . The magnitude of K_{AF} depends on the microstructure of the given material [28]. For this reason, we have studied the structure of our magnetron sputter deposited IrMn layers by XRD and HRTEM. The HRTEM image of an IrMn film containing embedded Ni-NPs is displayed in figure 2. The image shows the polycrystalline structure of the IrMn film with an average grain size of about 5 nm. The average grain size

calculated from the XRD peak width of the IrMn layer yields 6.5 ± 0.5 nm, and the crystal structure is fcc (not shown). The difference between the two values may be attributed to the fact that the XRD gives a volume weighted average size. Figure 3(a) shows a cross sectional TEM image of the films taken at a lower magnification. The Ni-NP positions have been detected by using energy filtered TEM (EFTEM, figure 3(b)). Due to the close contrast of Ni and Mn elements, and due to the low volume fraction of Ni (3%), it is difficult to obtain clear images of individual Ni particles. However, an image analysis of figure 3(b) gives us sizes of Ni-NPs between 4.8 and 13.8 nm in diameter, which is well within the range of Ni particle sizes shown in figure 1(a). The total film thickness is 200 nm. The interfaces between the individual IrMn layers deposited in each sequential deposition step show up as thin bright lines, which is possibly owing to a surface reconstruction process between the individual IrMn deposition sequences. The cumulative roughness of the layers most likely originates from the Ni-NPs in the matrix, as the initial roughness of the first layer is small. The diffractogram (the inset in figure 3(a)) also verifies the polycrystalline structure with some texturing of the IrMn matrix (encircled lattice reflections).

3.2. Exchange bias, coercivity and magnetic blocking

For a first test of the successful preparation of Ni-NP@IrMn, we field cooled the sample as described in the experimental section. Figure 4 shows the FC hysteresis measured at 10 K after field cooling. The results of the reference sample Ni-NP@SiO_x are also presented. While the reference has a narrow and symmetric hysteresis loop ($H_C = 122 \pm 20$ Oe) with small remanent magnetization, the Ni-NP@IrMn exhibits strongly enhanced $H_C = 974 \pm 20$ Oe and $H_{EB} = 821 \pm 20$ Oe. According to the Meiklejohn and Bean model we calculate the exchange energy density J_{ex} by taking the spherical interface into account [19],

$$J_{ex} = \mu_0 H_{ex} M_{FM} D_{FM} / 6. \quad (4)$$

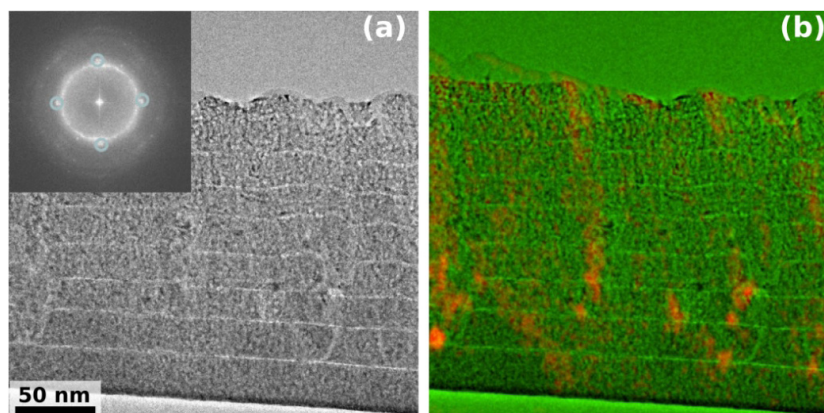


Figure 3. Energy filtered TEM image of the Ni-NP@IrMn matrix. (a) Cross sectional zero loss filtered (elastic scattered electrons) TEM image, the inset showing diffractogram; textured reflections of the IrMn matrix are encircled. (b) Composed image using zero loss TEM signal (green) and Ni $L_{2,3}$ absorption edge signal (red) to demonstrate the Ni distribution within the individual IrMn layers and the size of Ni-NPs.

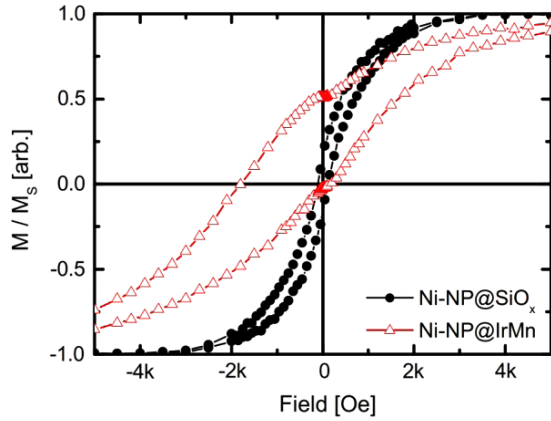


Figure 4. Hysteresis of Ni-NP@IrMn (Δ) and of Ni-NP@SiO_x (\bullet) after field cooling from 350 to 10 K in 50 kOe. Both loops were measured at 10 K in the field range of ± 50 kOe.

D_{FM} is the diameter of the FM particles coupled to the AF layer, and μ_0 is the vacuum permeability. For M_{FM} the bulk volume magnetization of Ni ($M_{\text{FM}} = 4.8 \times 10^5 \text{ A m}^{-1}$ [26]) is taken. We calculate $J_{\text{ex}} = 0.06 \text{ mJ m}^{-2}$ at 10 K. In previous reports, the J_{ex} of FM films coupled to IrMn with (111) texture has been found in the range of $0.01\text{--}0.19 \text{ mJ m}^{-2}$ ([17, 20] and references therein). J_{ex} strongly depends on the microstructure of IrMn, i.e. the degree of texture [29], the grain size [30, 31], and the composition of IrMn [22]. For example, Kohn *et al* [31] reported grain size-dependent J_{ex} values from highly textured CoFeB/Ir₂₂Mn₇₈ bilayers. Their results show good agreement with the present Ni-NPs in Ir₂₆Mn₇₄ films.

Training effect was observed in consecutive $M\text{--}H$ loops after an initial field cooling of the Ni-NP@IrMn from the *reference state* to 10 K (see figure S1 in the supplementary file available at stacks.iop.org/Nano/24/000000/mmedia). The effect is known to be a property of exchange coupled systems [32]. We found a 15% drop of H_{EB} after the first loop, after which it remains nearly constant. The observed behavior is similar to the behavior observed in other nanostructured exchange bias systems [33]. We studied the cooling field

dependence of H_{EB} and H_{C} of our Ni-NP@IrMn. For that purpose, we measured $M\text{--}H$ loops at 10 K after cooling the sample in different applied fields from 350 to 10 K (see figure S2 in the supplementary file available at stacks.iop.org/Nano/24/000000/mmedia). We found that the H_{EB} increases with increasing cooling field up to 5 kOe, then stays constant until 50 kOe. This agrees well with the saturation behavior of the particles, suggesting that the cooling field dependence of H_{EB} is mainly due to spin orientation in the FM.

In figures 5(a) and (b) the temperature dependences of H_{C} and H_{EB} of Ni-NP@IrMn and Ni-NP@SiO_x after a single field cooling process are shown. As expected, the H_{C} of both samples decreases with increasing temperature. A similar behavior is found for the H_{EB} of the NP@IrMn sample. A more striking observation is that the H_{C} of Ni-NP@IrMn at 200 K was around 200 ± 20 Oe, whereas for Ni-NP@SiO_x, it was only about 30 ± 20 Oe. At ambient temperature, we measured a value of $H_{\text{C}} = 70 \pm 20$ Oe for Ni-NP@IrMn, while the reference sample shows superparamagnetic behavior. In addition, figure 5(b) shows that there is a finite H_{EB} of 45 Oe at ambient temperature. These observations prove that Ni-NPs experience additional exchange coupling to the IrMn matrix, and that we were able to stabilize the magnetization of the initially superparamagnetic Ni-NPs even at ambient temperature.

In order to extract the blocking temperatures T_{B} of Ni-NP@IrMn and Ni-NP@SiO_x, we applied Sharrock's law [34]. The inset of figure 5(a) presents the temperature-dependent H_{C} data and a fit according to Sharrock's power law derived for single domain, randomly oriented, noninteracting particles,

$$H_{\text{C}}(T) = H_{\text{C}0} \left[1 - \left(\frac{T}{T_{\text{B}}} \right)^{2/3} \right] \quad (5)$$

where $H_{\text{C}0}$ is the coercive field H_{C} at 0 K. We can extract T_{B} values from equation (5) by a linear fit of H_{C} versus $T^{2/3}$. The result is shown in the inset of figure 5(a) and given for both samples in table 2. A comparison of the values of T_{B} obtained for the Ni-NP@IrMn and the Ni-NP@SiO_x clearly shows the stabilizing effect of the IrMn on the magnetization of the Ni-NPs.

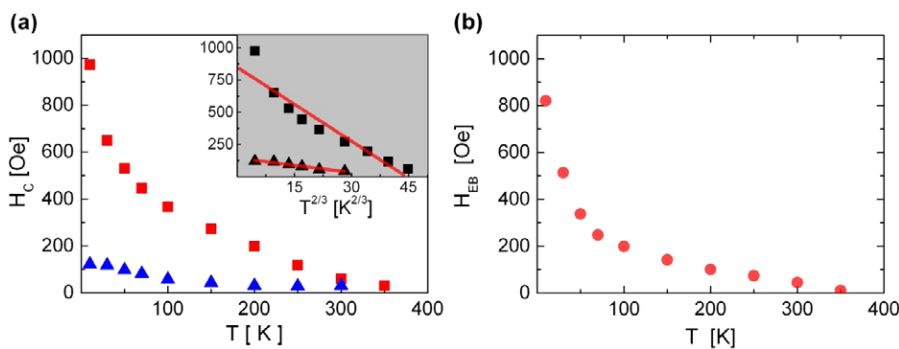


Figure 5. (a) Temperature dependence of the coercive field of Ni-NP@IrMn (\blacksquare) after field cooling to 10 K and the corresponding data of Ni-NP@SiO_x reference (\blacktriangle). The inset shows the fits according the Sharrock formula. Details are discussed in the text. (b) Temperature dependence of the exchange bias field of Ni-NP@IrMn after field cooling.

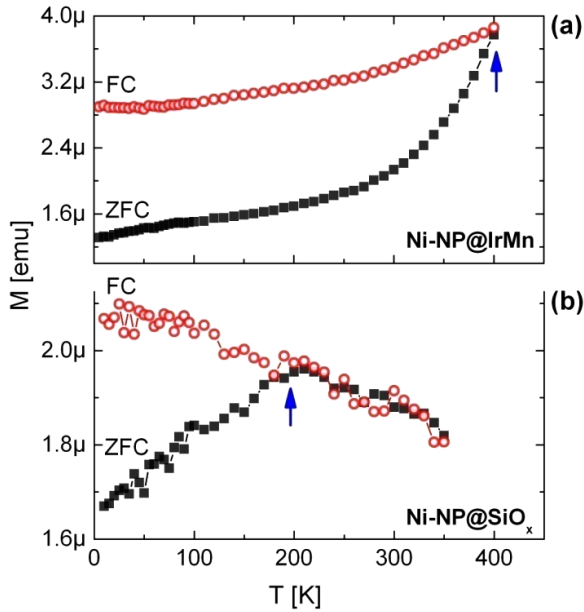


Figure 6. FC/ZFC curves of Ni-NP@IrMn (a) and Ni-NP@SiO_x (b). ZFC was measured by applying 20 Oe field after cooling to 10 K at zero field. The blue arrow indicates the maximum of the ZFC measurements.

Table 2. Extracted values from the fit of H_C versus $T^{2/3}$ using Sharrock's law over a temperature range from 10 to 300 K.

Property (units)	H_{C0} (Oe)	T_B (K)
Ni-NP@IrMn	826 ± 57	319 ± 17
Ni-NP@SiO _x	145 ± 6	240 ± 10

Standard ZFC/FC measurements as shown in figure 6 were conducted. The ZFC/FC curves from the Ni-NP@SiO_x reference sample (figure 6(b)) start to join around $T = 200 \pm 10$ K, indicating a T_B around this value. The broadness of the ZFC curve peak is due to the particle size distribution. On the other hand, the ZFC curve of the Ni-NP@IrMn (figure 6(a)) does not show the typical maximum around T_B in the accessible temperature range. Thus, we expect the blocking temperature to be slightly larger than 400 K.

Additional ZFC/FC curves at an applied field of 1000 Oe (not shown), however, show a distinct maximum around ambient temperature. It is known that the ZFC peak shifts to lower temperatures when the applied field increases [14, 27, 35]. The decreasing trend of the FC curves of Ni-NP@IrMn below T_B is typical for exchange coupled nanoparticles [33]. This behavior has been ascribed to the variation of the additional unidirectional exchange anisotropy with temperature. In summary, both the ZFC/FC measurements and the T_B values determined from Sharrock's law confirm the Ni-NP@IrMn to be still blocked at room temperature.

3.3. Magnetic relaxation of Ni-NP@IrMn

For a uniaxial system, one expects an exponential decay of the magnetization over time according to Néel relaxation

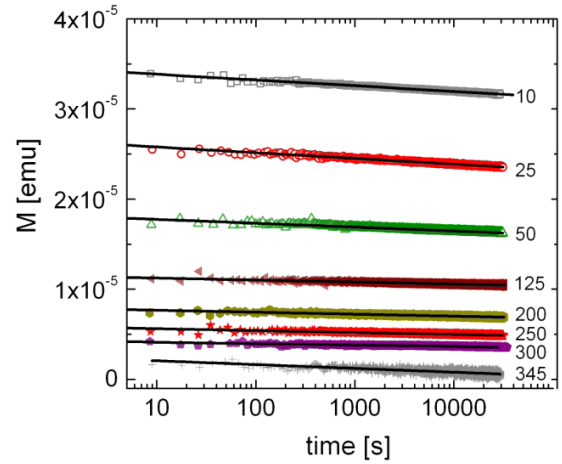


Figure 7. Thermo-magnetic relaxation of the remanent magnetization of Ni-NP@IrMn. The number assigned to each experimental curve is the measurement temperature in Kelvin, the same as T_{fc} . The solid lines are fits according to equation (6).

(equation (1)). However, in experiments, deviations from equation (1) are observed due to variations of the particle size, crystallographic orientations, the anisotropy, or magneto-static interactions of the particles. These effects result in a wide range of timescales in which an observable relaxation takes place [36]. Therefore, all have to be considered for a proper model. As early as 1949, Street and Woolley [37] proposed a flat distribution of anisotropy energies yielding a magnetization that decays logarithmically in time, when $t \geq 100$ s,

$$M(t) = M_0(1 - S \ln(t/\tau_0)) \quad (6)$$

where S is the so-called magnetic viscosity, and M_0 is the initial magnetization [36]. The model is useful for understanding the long-time behavior of magnetic systems like recording media, and has been used in many similar cases since then [38–40].

Figure 7 shows the relaxation behavior of Ni-NP@IrMn after FC from the *reference state* to T_{fc} (number at the end of each line). The straight lines are linear fits according to equation (6), clearly proving the logarithmic decay. The slope is proportional to the magnetic viscosity S at a given temperature T_{fc} . In figure 8, we show the resulting values of S as function of temperature. In the range of 10–300 K, S is small and weakly temperature-dependent. At temperatures above 300 K, S increases significantly. From these measurements, we can conclude that the magnetization of the embedded particles is relatively stable up to this temperature. Stabilization of Co nanoparticles by the effect of an antiferromagnetic matrix on the energy barrier has already been demonstrated by Skumryev *et al* [7].

According to Kodama [40], S is associated with the energy barrier distribution $n(\bar{E})$ through the relationship

$$S = n(\bar{E})k_B T \quad (7)$$

where \bar{E} is the mean energy barrier which has to be overcome to reverse the particle magnetization within the experimental

Q.8

Q.9

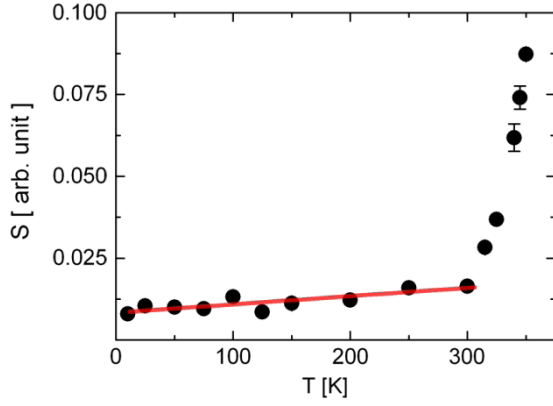


Figure 8. Temperature dependence of the viscosity S taken from the relaxation measurements after FC. The line is the linear fit in the range of 10–300 K.

Q.10 window. As explained in [40], the experimental window sweeps over parts of $n(E)$ as the temperature is changed. According to equation (7), a linear S versus T curve indicates a constant barrier distribution over a range of energies [40]. Experimental results from non-embedded Co nanoparticles with mean diameter of 6.9 nm show a curved $n(\bar{E})$ within a temperature range of 80–150 K [39]. On the other hand, in the case of core-shell Co/CoO nanoparticles with 6 nm diameter, a linear S versus T is observed over a temperature range of 8 K $< T < 50$ K [33]. In view of these results, we believe that the linear S versus T curve observed for our Ni-NP@IrMn system is also related to the additional contribution of the antiferromagnetic IrMn matrix to the anisotropy energy.

3.4. Effect of field cooling temperature on H_C and H_{EB}

As explained in the experimental section, quantitative modeling of the exchange bias can only be performed when relaxation effects in the AF film are minimized. In this section, we used the modified protocol in which the sample was cooled to 10 K after field cooling to T_{fc} , and immediately measured at 10 K.

As shown in figure 9(a), the exchange bias field H_{EB} strongly depends on T_{fc} : it drops from 821 ± 20 Oe to 120 ± 20 Oe when the T_{fc} is changed from 10 to 300 K. In order to elucidate the dependence of H_{EB} on T_{fc} , the model suggested by O'Grady *et al* [30] is applied. The group studied CoFe (2.5 nm) thin films coupled to polycrystalline IrMn underlayers with different average IrMn grain sizes ranging from 4.5 to 15 nm. Their results show that the exchange bias field depends on the grain size of the IrMn. The approach used in [30] is based on the model of Fulcomer and Charap [41], which considers the effect that small AF grains exhibit superparamagnetic behavior above a blocking temperature which depends on the grain size. Below a certain critical grain volume V_c , there is no stable AF ordering due to thermal fluctuations during the measurement time t_{meas} . If the grain volume gets too large, the anisotropy energy of the grain will increase so much that it becomes difficult to set the grains within a finite time t_{set} at a given temperature. The actual temperature T_{set} at which the field cooling is started determines the upper limit of grain volume V_{set} which can be set. The exchange bias can then be calculated by considering only the contributions of IrMn grains in the volume range between V_c and V_{set} ,

$$H_{EB}(T_{fc}) = H' \int_{V_c}^{V_{set}} f(V) dV \quad (8)$$

where $f(V)$ is a log-normal like grain volume distribution function. H' is a constant which is related to interface exchange coupling. The volume size window can be easily estimated using equation (1) and replacing τ_N by the measurement time t_{meas} ,

$$V_c = \frac{\ln(t_{meas}/\tau_0)k_B T_{fc}}{K_{IrMn}(T_{fc})}, \quad (9)$$

$$V_{set} = \frac{\ln(t_{set}/\tau_0)k_B T_{set}}{K_{IrMn}(T_{set})}.$$

Taking $K_{IrMn}(T)$ values from [29], we get $V_c(300 \text{ K}) = 207 \text{ nm}^3$ and $V_{set} = 320 \text{ nm}^3$ ($t_{meas} = 100 \text{ s}$, $t_{set} = 3600 \text{ s}$, $T_{set} = 350 \text{ K}$, K_{IrMn} as $4.4 \times 10^5 \text{ J m}^{-3}$ at 350 K and $5.1 \times 10^5 \text{ J m}^{-3}$ at 300 K, respectively). These values

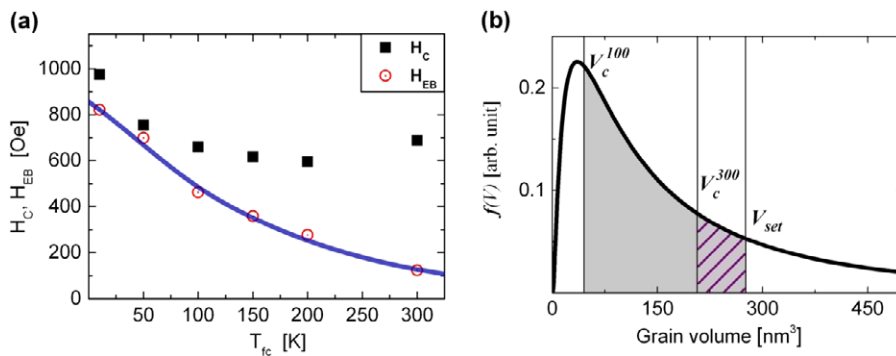


Figure 9. (a) The effect of the field cooling temperature, T_{fc} , on the H_C and H_{EB} of Ni-NP@IrMn when measured at 10 K. Error bars are within the symbols. The solid blue curve is a calculated curve using equation (8). (b) The estimated IrMn grain volume distribution curve of our sample; the integrated area between V_c and V_{set} corresponds to the fraction of grains which are exchange coupled to Ni-NPs after FC.

correspond to spherical grain sizes of $D_c = 7.3$ nm (critical grain size at 300 K) and $D_{set} = 8.1$ nm. For our sample, taking the HRTEM and XRD results into account, we have estimated a log-normal IrMn grain size distribution with 4.8 nm mean size and $\sigma = 0.4$ (similar to the one reported in [42]). Since each T_{fc} sets different V_c , the volume range over which we have to integrate will be different for each T_{fc} , as depicted in figure 9(b), showing V_c positions at 100 and 300 K. By choosing an appropriate constant factor (H') (see equation (8)), we get the $H_{EB}(T_{fc})$ curve shown in figure 9(a). The model curve fits to the experimental observations quite accurately. We conclude that the dependence of H_{EB} on T_{fc} can be well described by this approach, which is based on the assumption of individual AF grains being coupled to the FM, but not with each other [41].

The basic characteristics of exchange bias in nanostructures are a hysteresis loop shift, expressed by H_{EB} , and a coercivity enhancement [16]. In the case of low anisotropy energy of the AF, the coercivity enhancement can be associated with spin rotation in the AF grains. However, when the AF has high anisotropy energy (which is perhaps closer to the actual situation in the Ni/IrMn system), the coercivity will rather be determined by the energy necessary to form a domain wall [43]. Large enhancements in H_C have been previously observed in exchange coupled nanostructures [7] and attributed to an increase in the energy barrier against rotation of the magnetization. The coercivity enhancement is closely related to stabilization of the magnetization of the nanoparticles, which is the most important effect for data storage applications. Therefore, we have studied the influence of T_{fc} on coercivity enhancement in our samples.

In figure 9(a) the dependence of H_C on T_{fc} is shown. H_C is 974 ± 20 Oe for $T_{fc} = 10$ K, and decreases to 660 ± 20 Oe for $T_{fc} = 100$ K. In the range of T_{fc} between 100 and 300 K, we find an average H_C of 640 Oe. Apparently, in this temperature range we always observe a similar contribution of the IrMn to the energy barrier regardless of the variation of the fraction of 'set' IrMn grains.

The decrease of H_C for T_{fc} between 10 and 100 K indicates that the energy barrier also decreases. According to equation (9), a T_{fc} of 100 K corresponds to a critical IrMn grain size of 4.5 nm. This value is not only comparable to the mean grain size of our IrMn films, but also similar to the exchange correlation length (which is closely related to the domain wall thickness [16]) of IrMn, which was found to be 4 nm in bilayer studies [44]. A possible explanation for the observed energy barrier decrease is suggested by the random anisotropy model for nanocrystalline ferromagnetic materials [45]. In that model, the effective anisotropy energy barrier (which determines the coercivity) is reduced by averaging over the energy contributions of many individual, randomly oriented nanocrystals in a volume determined by the exchange correlation length. For a T_{fc} of 100 K or more, the AF spins in a significant fraction of IrMn grains will have no preferred orientation. We may expect a similar effect of averaging over the contributions of individual IrMn grains within the volume defined by a shell centered on the Ni-NPs with a thickness comparable to the exchange

correlation length. We note that this is not in contradiction to the assumption that the AF grains are magnetically uncoupled with respect to each other, since here the averaging takes place through the interaction of individual IrMn grains with the FM Ni-NPs. On the other hand, for a T_{fc} below 100 K, the grains within this shell will have their AF spins frozen in directions determined by the external applied field, so that the averaging over different grains leads to no significant reduction of the energy barrier.

4. Conclusion

We have successfully prepared 8.4 nm Ni-NPs with narrow size distribution embedded in a polycrystalline IrMn film. A strong exchange coupling between ferromagnetic Ni-NPs and antiferromagnetic IrMn film was observed despite the lack of an epitaxial relation between them. At 300 K, we still observed a stable magnetization of the Ni-NPs embedded in IrMn, whereas Ni-NPs embedded in SiO_x show superparamagnetic behavior under these conditions. The exchange energy density calculated using the Meiklejohn and Bean model at 10 K was found to be similar to the values of IrMn bilayer systems in the literature. The thermo-magnetic relaxation curves confirm that the particles are magnetically stable in the temperature range of 10–300 K. This is attributed to the contribution of the IrMn to the energy barrier against rotation of the magnetization in the Ni particles. By applying a field cooling protocol which minimizes magnetic relaxation of the IrMn grains, we have been able to describe the influence of the field cooling procedure on H_{EB} . We also find an effect of the field cooling temperature on H_C below 100 K, which appears to be related to the exchange correlation length of the IrMn. The results of our study indicate that stabilization of ferromagnetic nanoparticles at ambient temperature may be achieved by embedding them in IrMn films, which makes the system interesting for applications.

Acknowledgment

Parts of the work have been financed by Baden-Württemberg Stiftung in the framework of the 'Functional Nanostructures' program.

References

- [1] Sun S, Murray C B, Weller D, Folks L and Moser A 2000 *Science* **287** 1989
- [2] Kools J 1996 *IEEE Trans. Magn.* **32** 3165
- [3] Tartaj P, Morales M, Veintemillas-Verdaguer S, González-Carreño T and Serna C 2003 *J. Phys. D: Appl. Phys.* **36** R182
- [4] Pankhurst Q A, Connolly J, Jones S K and Dobson J 2003 *J. Phys. D: Appl. Phys.* **36** R167
- [5] Lu A, Salabas E and Schüth F 2007 *Angew. Chem.* **46** 1222
- [6] Dave S R and Gao X 2009 *Wiley Interdiscip. Rev.-Nanomed. Nanobiotechnol.* **1** 583
- [7] Skumryev V, Stoyanov S, Zhang Y, Hadjipanayis G, Givord D and Nogués J 2003 *Nature* **423** 850
- [8] Nogués J, Sort J, Langlais V, Doppiu S, Dieny B, Muñoz J, Suriñach S, Baró M, Stoyanov S and Zhang Y 2005 *Int. J. Nanotechnol.* **2** 23

- [9] Pati S, Bhushan B, Basumallick A, Kumar S and Das D 2011 *Mater. Sci. Eng. B* **176** 1015
- [10] Binns C et al 2010 *J. Phys.: Condens. Matter.* **22** 436005
- [11] Sahoo S, Binek C and Kleemann W 2003 *Phys. Rev. B* **68** 174431
- [12] Tobia D, Winkler E, Zysler R D, Granada M, Troiani H E and Fiorani D 2009 *J. Appl. Phys.* **106** 103920
- [13] Laureti S, Peddis D, Bianco L D, Testa A, Varvaro G, Agostinelli E, Binns C, Baker S, Qureshi M and Fiorani D 2012 *J. Magn. Magn. Mater.* **324** 3503
- [14] Wiedwald U, Lindner J, Spasova M, Frait Z and Farle M 2005 *Phase Transit.* **78** 85
- [15] Nogués J, Skumryev V, Sort J, Stoyanov S and Givord D 2006 *Phys. Rev. Lett.* **97** 157203
- [16] Nogués J, Sort J, Langlais V, Skumryev V, Suriñach S, Muñoz J and Baró M 2005 *Phys. Rep.* **422** 65
- [17] Waser R (ed) 2003 *Nanoelectronics and Information Technology* (New York: Wiley-VCH)
- [18] Nogués J and Schuller I K 1999 *J. Magn. Magn. Mater.* **192** 203
- [19] Meiklejohn W H and Bean C P 1957 *Phys. Rev.* **105** 904
- [20] Grünberg P A 2001 *Sensors Actuators A* **91** 153
- [21] Saranu S, Selve S, Kaiser U, Han L, Wiedwald U, Ziemann P and Herr U 2011 *Beilstein J. Nanotechnol.* **2** 268
- [22] Hoshino K, Nakatani R, Hoshiya H, Sugita Y and Tsunashima S 1996 *Japan. J. Appl. Phys.* **35** 607
- [23] Hoffmann A 2004 *Phys. Rev. Lett.* **93** 097203
- [24] Hihara T and Sumiyama K 1998 *J. Appl. Phys.* **84** 5270
- [25] Sun S 2006 *Adv. Mater.* **18** 393
- [26] Jiles D 1998 *Introduction to Magnetism and Magnetic Materials* (New York: Taylor and Francis)
- [27] Sappey R, Vincent E, Hadacek N, Chaput F, Boilot J P and Zins D 1997 *Phys. Rev. B* **56** 14551
- [28] Buschow K H J (ed) 2006 *Handbook of Magnetic Materials* (Amsterdam: Elsevier B.V.)
- [29] van Driel J, de Boer F R, Lenssen K-M H and Coehoorn R 2000 *J. Appl. Phys.* **88** 975
- [30] O'Grady K, Fernandez-Outon L and Vallejo-Fernandez G 2010 *J. Magn. Magn. Mater.* **322** 883
- [31] Kohn A, Dean J, Kovacs A, Zeltser A, Carey M J, Geiger D, Hrkac G, Schrefl T and Allwood D 2011 *J. Appl. Phys.* **109** 083924
- [32] Paccard D, Schlenker C, Massenet O, Montmory R and Yelon A 1966 *Phys. Status Solidi* **16** 301
- [33] Peng D L, Sumiyama K, Hihara T, Yamamuro S and Konno T J 2000 *Phys. Rev. B* **61** 3103
- [34] Sharrock M P 1994 *J. Appl. Phys.* **76** 6413
- [35] Thomas S, Uhlig M, Wiedwald U, Han L, Ziemann P and Albrecht M 2013 *Nanotechnology* **24** 155703
- [36] Majetich S A and Sachan M 2006 *J. Phys. D: Appl. Phys.* **39** R407
- [37] Street R and Woolley J C 1949 *Proc. Phys. Soc. A* **62** 562
- [38] O'Grady K 1990 *IEEE Trans. Magn.* **26** 1870
- [39] O'Grady K and Chantrell R W 1986 *J. Magn. Magn. Mater.* **54–57** 757
- [40] Kodama R H 1999 *J. Magn. Magn. Mater.* **200** 359
- [41] Fulcomer E and Charap S H 1972 *J. Appl. Phys.* **43** 4190
- [42] Vallejo-Fernandez G, Deakin T, O'Grady K, Oh S, Leng Q and Pakala M 2010 *J. Appl. Phys.* **107** 09D709
- [43] O'Handley R C 1999 *Modern Magnetic Materials—Principles and Applications* (New York: Wiley)
- [44] Ali M, Marrows C H, Al-Jawad M, Hickey B J, Misra A, Nowak U and Usadel K D 2003 *Phys. Rev. B* **68** 214420
- [45] Herzer G 1989 *IEEE Trans. Magn.* **25** 3327